Uncertainty Quantification of Shock-Bubble Interaction

By K. K. So, T. Chantrasmi†, X. Y. Hu, C. Stemmer, G. Iaccarino† AND N. A. Adams

Lehrstuhl für Aerodynamik und Strömungsmechanik, Technische Universität München
Boltzmannstr. 15, 85748 Garching b. München

In this work, we extend our previous uncertainty analysis of shock-bubble interactions based on an experimental case of helium-air shock-bubble interaction. The uncertainty of the inhomogeneity of the contaminating air inside the helium bubble is formulated as a new uncertainty parameter. The interface evolution and the total vorticity are considered as the quantities of interest. The gas inhomogeneity along the spanwise direction inside the bubble introduces a flow asymmetry along the streamwise direction. The variance in the initial bubble is found to be transported and amplified as the interface evolves. The vortex position of the rolled-up bubble is found to be the region of the maximum variance of density. The total vorticity under different gradients of gas inhomogeneity is compared with those under different bubble shape and different amount of gas contamination. As compared with the analytical and numerical analysis of baroclinic vorticity production for a homogeneous circular bubble in shock-bubble interaction in reference literature, the baroclinic vorticity generation during the vorticity deposition phase is found to be largely dependent on the gas inhomogeneity inside the bubble and the windward length of the bubble when uncertainties of the initial bubble condition are present.

1. Introduction

Based on our previous work on the uncertainty analysis of shock-bubble interactions [1], we aim at extending the analysis to a new uncertainty parameter.

The primary objective of uncertainty analysis is to quantify the uncertainties present in experiments, which exist inevitably due to the variation in test conditions and limited reproducibility of the experiment setup and conditions. For shock-bubble interactions, the experimental condition of the bubble is one of the main sources of variation and thus uncertainty. As an example, the test gas impurity inside the bubble is present in many shock-bubble interaction experiments, whether the membrane or membraneless bubble formation technique is used. The problem of the test gas impurity has been addressed previously, for example in [2]. It is shown that the effect of an uncertain amount of acetone (added to the bubble gas for experimental image tracing purposes) on the evolution of the Richtmyer-Meshkov Instability (RMI) and mixing in an air-SF6 shock-bubble interaction is not negligible as demonstrated by means of a series of numerical simulations.

In [1], the uncertainty parameters of the bubble deformation and the degree of air

† Center for Turbulence Research, Stanford University, CA 94305, USA

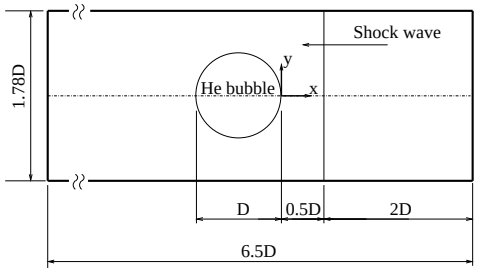

FIGURE 1. Schematic of the computational domain for the shock-bubble interaction simulation. The helium bubble diameter, D, is $50mm$.

contamination in the helium bubble were formulated, and the quantities of interest including the interface evolution and the primary vorticity generation were studied. The uncertainty of the amount of contamination was studied under the assumption that the contaminating gas is evenly distributed inside the bubble. However, as observed from the images of the bubble initial condition in the experimental literature, the gas mixture is not necessarily homogeneous. For example in [3], when the bubble is formed in the shock tube, the heavy gas tends to concentrate on one end of the bubble due to gravity, leading to gas inhomogeneity inside the bubble, and in some cases also to the deformation of the bubble. Therefore, the current study aims to extend the previous work in [1] to a new uncertainty parameter, which is the inhomogeneity of the bubble gas mixture, i.e., the mixture of helium and the contaminating air.

The paper is organized as follows: in the section of preliminaries, the shock-bubble interaction studied, the definition of the uncertainty parameter and the quantities of interest are described. Then, the governing equations and the numerical methods of the flow solver, and the uncertainty quantification methods are explained. The statistic of the two quantities of interest are presented, followed by the discussions of the variance in interface evolution and the baroclinic vorticity generation.

2. Preliminaries

2.1. *Air-helium shock-bubble interaction*

As in [1], the experimental case of a cylindrical-helium-bubble in air hit by a shock wave at Mach number of 1.22 of [4] serves as the base case for our investigation.

The case setup from [1] is adopted, except in the current study no symmetry along the centerline in the streamwise direction is assumed, as it is expected that the gas inhomogeneity along the spanwise direction would introduce asymmetric flow patterns. The computational domain is shown in Fig. 1.

2.2. *Uncertainty parameter*

The uncertainty parameters are defined based on the available information from the experimental literature, and in addition generalized to describe the generic uncertainties present in shock-bubble interaction experiments. In [4], the authors reported that the helium-cylinder was contaminated by 28% air (by mass). The estimation of the air contamination is subject to experimental measurement errors, and when they are taken into account, the range of the air contamination is found to be $[48.38\%, 5.87\%]$. This uncertainty parameter of the air contamination, f^{air}_{mass}, has been studied in [1] under the assumption that the contaminating air is homogeneously distributed inside the bubble.

Another uncertainty parameter which is generic to describe the bubble deformation – eccentricity, e – has also been studied in [1]. The range of e is taken in the interval $[-0.5, +0.5]$ which describes a bubble of an elliptic shape with its axis along the streamwise direction varying. The amount of air contamination of 28% by mass is maintained in the range of e.

In this paper, we extend the study of the uncertainty of air contamination to gas inhomogeneity. While fixing the air contamination to 28% by mass, we assume a gas inhomogeneity inside the bubble, f_{in}^{air}. This uncertainty parameter aims to mimic the uncertainty of the initial distribution of the contaminating gas in the bubble, which can be present in shock-bubble interaction experiments, for example [3]. By keeping the same amount of air inside the bubble and assuming the inhomogeneity gradient is along the spanwise direction, the range of f_{in}^{air} is defined as $[0, 1]$, where the two extreme cases and the middle case are:

– $f_{in}^{air} = 0$: the extreme case where no inhomogeneity is assumed, i.e., the contaminating air is evenly distributed in the bubble.

– $f_{in}^{air} = 1$: the extreme case where the maximum inhomogeneity is assumed, i.e., pure helium is on one end of the bubble.

– $f_{in}^{air} = 0.5$: the middle case where a certain inhomogeneity is assumed.

The density plots of these cases are shown in Fig. 4.

2.3. *Quantity of interest*

Two quantities of interest, namely the interface evolution and the total vorticity, are considered in this study.

2.3.1. *Interface evolution*

For code verification purposes, the interface evolution is an important quantity of interest for the comparison between different numerical results as well as comparison with the experimental results [5]. On the other hand, the interface evolution is also studied extensively by experiments, for example in [3] different geometries of the shocked bubble under different gas pairs were recorded for characterizing the shock-bubble interactions. In [1] the characteristic interface points, namely the upstream location, the downstream location and the jet of the interface, are used to characterize the interface evolution. Here in our study of the uncertainty of the gas inhomogeneity, as the flow pattern along the streamwise direction is expected to be asymmetrical, the interface evolution can no longer be represented by the characteristic interface points. Moreover, as shown below in Sec. 4, the maximum variance is located at the vortex position which cannot be measured by the characteristic interface points. Therefore, to examine the interface evolution on the whole flow field, the plot of density and Schlieren-type images, $|\nabla\rho|$, are used to illustrate the interface evolution.

2.3.2. *Total vorticity*

The other quantity of interest is the total vorticity, Γ, which is defined as the integration of the magnitude of vorticity over the domain:

$$\Gamma = \int |\omega| \, dxdy \quad , \tag{2.1}$$

where ω is the vorticity defined as $\nabla \times \mathbf{v}$, and $\mathbf{v}$ is the velocity. During the early time of shock-bubble interactions, the total vorticity measures the baroclinic vorticity production due to the misalignment of the pressure gradient and the density gradient.

3. Methods

3.1. *Governing equations and numerical methods of fluid simulation*

To simulate the shock-bubble interaction, a two-phase compressible flow algorithm is adopted. The Euler equations, without the surface tension, are used for the shock-bubble interaction simulation. The volume-of-fluid (VOF) interface-capturing method is employed, and the two phases are represented by their volume fractions, where the formulation of the volume-fraction transport equations of [6] is adopted. A single-velocity, pressure-equilibrium, six-equation model is obtained as follows:

$$\frac{\partial \alpha}{\partial t} + \nabla \cdot \alpha \mathbf{u} = \alpha \frac{\overline{K}_S}{K_S^\alpha} \nabla \cdot \mathbf{u} \quad , \tag{3.1}$$

$$\frac{\partial \beta}{\partial t} + \nabla \cdot \beta \mathbf{u} = \beta \frac{\overline{K}_S}{K_S^\beta} \nabla \cdot \mathbf{u} \quad , \tag{3.2}$$

$$\frac{\partial \alpha \rho^\alpha}{\partial t} + \nabla \cdot \alpha \rho^\alpha \mathbf{u} = 0 \quad , \tag{3.3}$$

$$\frac{\partial \beta \rho^\beta}{\partial t} + \nabla \cdot \beta \rho^\beta \mathbf{u} = 0 \quad , \tag{3.4}$$

$$\frac{\partial \rho \mathbf{u}}{\partial t} + \nabla \cdot \rho \mathbf{u}\mathbf{u} + \nabla p = 0 \quad , \tag{3.5}$$

$$\frac{\partial \rho E}{\partial t} + \nabla \cdot \left(\rho E + p \right) \mathbf{u} = 0 \quad , \tag{3.6}$$

where α and β are the volume fractions of the two phases respectively, t is the time, $\mathbf{u}$ is the velocity, $\overline{K}_S$ is the mixture bulk modulus, K_S^α and K_S^β are the phase bulk moduli, ρ^α and ρ^β are the phase densities, p is the pressure and E is the total energy.

Both phases are described by the ideal-gas equation of state (EOS) which reads

$$p = \left(\gamma - 1 \right) \rho e \quad , \tag{3.7}$$

where e is the internal energy and γ is the heat capacity ratio.

The volume-fraction equations are discretized by a volume-fraction adjustment corresponding to the compressibility effect [6]. The HLL Riemann solver [7] is adopted for the flux calculation and the reconstruction of the variables at the cell face are calculated by the van Leer MUSCL scheme. The time derivative is discretized by a third-order TVD Runge-Kutta scheme where the time step is determined by the CFL requirement with a CFL number of 0.2.

In order to verify our simulation code, and to demonstrate the quantities of interest computed are accurate, we conduct a grid-convergence study and compare the result with other established numerical results for the base deterministic case simulated by reference literature. In Fig. 2, the characteristic interface points converge as the grid refines, and by comparing the results with that of [5], it can be seen that the evolution of the characteristic interface points in the two simulations are in good agreement. In Fig. 3, Γ converges upon the refinement of the grid for $t = 0 - 150 \mu s$. The evolution of Γ also agrees with the observations of [8] where Γ bottoms out at around $t = 60 \mu s$, which is the moment when the refracted wave emerges from the bubble. For $t = 0 - 60 \mu s$, the shock front traverses one bubble-radius distance, i.e., it sweeps through the windward side of the bubble.

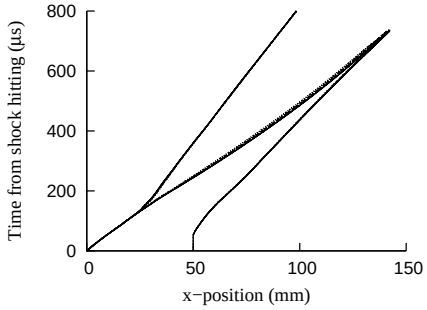

FIGURE 2. Space-time diagrams for three characteristic interface points. Solid line, $\Delta x/D = 0.0025$, dashed line, $\Delta x/D = 0.005$; dotted line, $\Delta x/D = 0.01$.

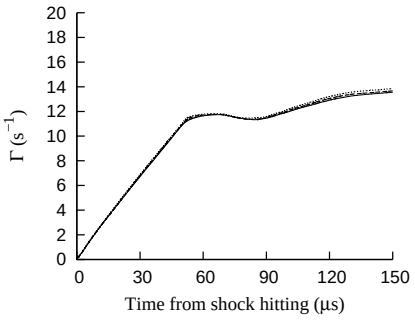

FIGURE 3. Total vorticity against time. Solid line, $\Delta x/D = 0.0025$, dashed line, $\Delta x/D = 0.005$; dotted line, $\Delta x/D = 0.01$.

3.2. *Uncertainty quantification method*

The uncertainty quantification can be categorized into three areas: i) data assimilation, ii) uncertainty propagation, and iii) output certification. In this work we focus on the uncertainty propagation, where by assuming a Probability Density Function (PDF) of the uncertainty parameter, the statistic and the PDF of the quantities of interest can be studied. The Monte Carlo method, the Stochastic Collocation method and the Stochastic Galerkin method are the principal methods for the uncertainty propagation. The Stochastic Collocation method, which is based on a probabilistic analysis, is adopted for the uncertainty quantification of this work. The output statistics are obtained from a limited number of deterministic calculations by the flow solver.

First, the uncertainty parameter is converted into a random variable. Since the distribution of the input uncertainty parameter is not available from the experimental literature, it is assumed to be uniform in the range of the uncertainty parameter. Given a distribution of the uncertainty parameter the evolution of the PDF of the quantities of interest can be studied. To identify the regions that correspond to the propagation and the amplification of the input variance, the mean and variance fields of the quantities of interest in physical space are constructed.

Let $u(\vec{x}, t, \vec{\xi}(\omega))$ be the output quantity of interest where $\vec{\xi}(\omega)$ is the uncertainty parameter. $\{\Psi_k(\vec{\xi}(\omega))\}, k \in \mathbb{N} \cup \{0\}$ denotes a set of orthogonal polynomials, where $\mathbb{N}$ is set of natural numbers. The orthogonality condition is expressed as

$$\langle \Psi_i(\vec{\xi}), \Psi_j(\vec{\xi}) \rangle = \delta_{ij} \quad , \tag{3.8}$$

where δ_{ij} is the Kronecker delta and $\langle \cdot, \cdot \rangle$ denotes the inner product with respect to specific weights.

These weights depend on the choice of the polynomial basis, e.g. the weights are uniform for Legendre polynomials and $(1-x^2)^{-\frac{1}{2}}$ for the Chebyshev polynomials.

The polynomial chaos expansion (PCE) of the random quantity, u is given by

$$u(\vec{x}, t, \vec{\xi}(\omega)) = \sum_{k=0}^{\infty} u_k(\vec{x}, t)\Psi_k(\vec{\xi}(\omega)) \quad , \tag{3.9}$$

where the $\{u_k\}$ are called the PCE coefficients. By the Cameron-Martin theorem, this series converges in the L-2 sense. Thus, we can approximate u with a finite number of terms:

$$u(\vec{\xi}) \approx \sum_{k=0}^{N} u_k \Psi_k(\vec{\xi}) \quad , \tag{3.10}$$

where the explicit dependences on $\vec{x}$, t, and ω are dropped from the notation for compactness. To approximate u, the coefficients can be computed by a projection using the orthogonality property stated above:

$$u_k = \langle u(\vec{\xi}), \Psi_k(\vec{\xi}) \rangle \quad . \tag{3.11}$$

The evaluation of the inner products above requires a numerical integration because u is not known at all $\vec{\xi}$. There are two popular choices of numerical integration rules: Gauss and Clenshaw-Curtis quadrature. The former is the most accurate in term of polynomial exactness (ability to integrate exactly polynomial of a given order), whereas the latter is more advantageous for practical applications because of its nestedness property, i.e one can reuse the data from low-ordered estimates as part of the higher-ordered ones. In this work, we choose Clenshaw-Curtis quadrature.

To summarize, we calculate the PCE coefficients from Eq. (3.11) by performing deterministic numerical simulations corresponding to the quadrature abscissas. The results is used for obtaining an approximation of u based on Eq. (3.10). The statistic of the output can then be extracted.

Additionally, we selected the polynomial basis – Legendre polynomials – in the approximation corresponding to the input distributions f_ξ - uniform random variables so that we can compute the mean and variance of u explicitly.

The mean, $\mathbb{E}(u)$, and the variance, $\mathsf{Var}(u)$, of u are obtained by

$$\mathbb{E}(u) = \int u f_\xi d\vec{\xi} \approx \sum_{k=0}^{N} u_k \left(\int \Psi_k f_\xi d\vec{\xi} \right) = u_0 \quad , \tag{3.12}$$

$$\mathbb{E}(u^2) = \int u^2 f_\xi d\vec{\xi} \approx \sum_{k=0}^{N}\sum_{i=0}^{N} u_k u_i \left(\int \Psi_k \Psi_i f_\xi d\vec{\xi} \right) = \sum_{k=0}^{N} u_k^2 \quad , \tag{3.13}$$

$$\mathsf{Var}(u) = \mathbb{E}(u^2) - \mathbb{E}(u)^2 = \sum_{k=1}^{N} u_k^2. \tag{3.14}$$

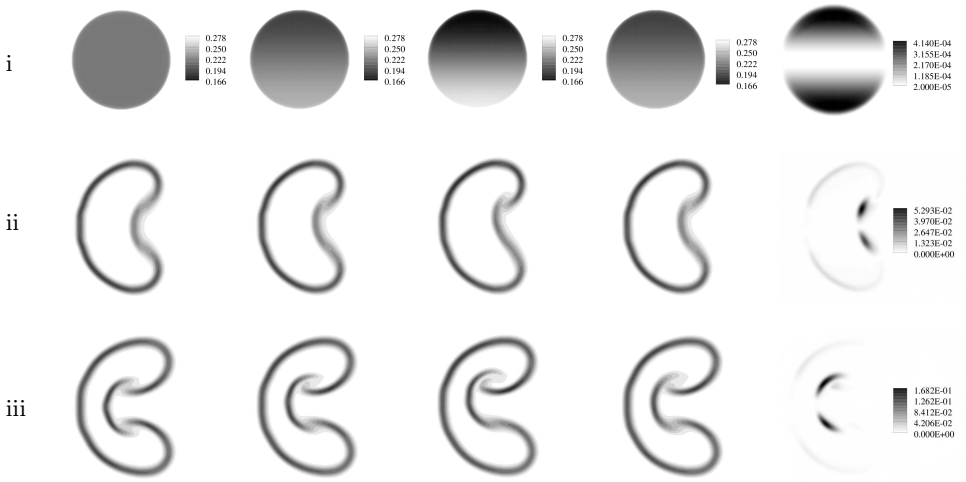

FIGURE 4. Interface evolution. Rows from top to bottom: i) density plots showing the initial conditions of the bubble, ii) $|\rho|$ showing the interface location at $245\ \mu s$ after the shock impact, iii) $|\rho|$ at $427\ \mu s$ after the shock impact. The left three columns are the individual cases under $f_{in}^{air} \in [0, 1]$, from left to right: i) $f_{in}^{air} = 0$, ii) $f_{in}^{air} = 0.5$, iii) $f_{in}^{air} = 1$. The right two columns are the collocated results, from left to right: i) mean of density, ii) variance of density.

4. Results and discussions

The results are presented and discussed according to the two qualities of interest, namely the interface evolution and the total vorticity.

4.1. *Interface evolution*

The interface evolution of the two extreme cases in the range of the uncertainty parameter of the gas inhomogeneity, $f_{in}^{air} \in [0, 1]$, and of the middle case are shown in the three leftmost columns in Fig. 4. The collocated results, namely the plot of the mean and the variance of density are shown in the two rightmost columns in the same figure.

The uncertainty quantification measures the statistic of the quantities of interest due to the uncertainty in the initial condition. The mean position of the interface location and locations of maximum variance at different time instants can be studied as shown in Fig. 4.

As can be seen in Fig. 4, under the uncertain parameter f_{in}^{air} the location of the maximum variance is near the vortex at late times. This is consistent with the comparison of individual deterministic cases (see $f_{in}^{air} = 0$ and $f_{in}^{air} = 1$ in Fig. 4) where the interface roll-ups and evolutions are different due to different gradients of gas inhomogeneity. The main difference of asymmetrical flow patterns in the streamwise direction is shown by the variance in interface evolution by the collocated results. In contrast, the maximum variance of the interface evolution under the uncertainties e and f_{mass}^{air} is near the jet location [1] (The impinging air into the helium bubble along the streamwise axis).

When we replot the variance of density in log-scale as shown in Fig. 5, it can be seen that the variance in the initial condition is transported and amplified to later times.

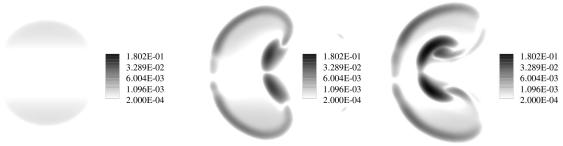

FIGURE 5. Variance in interface evolution. The variance of density plotted in log-scale at three time instants, from left to right: i) initial condition, ii) at $245\ \mu s$ after the shock impact, iii) at $427\ \mu s$ after the shock impact.

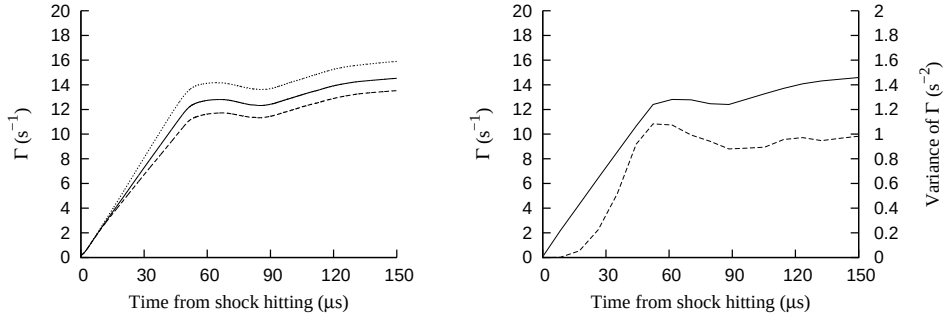

FIGURE 6. Total vorticity. Left: individual cases under $f_{in}^{air} \in [0, 1]$, dashed line – $f_{in}^{air} = 0$, solid line – $f_{in}^{air} = 0.5$, dotted line – $f_{in}^{air} = 1$. Right: collocated results, solid line – mean of Γ, dashed line – variance of Γ.

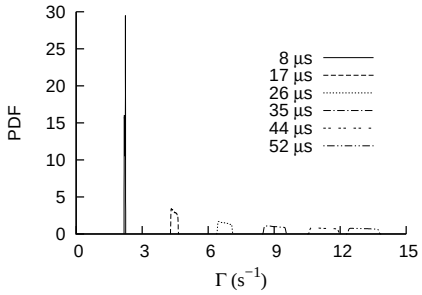

FIGURE 7. PDF of total vorticity as a function of time.

4.2. *Total vorticity*

The total vorticity of the two extreme cases in the range of the uncertainty parameter of the gas inhomogeneity, $f_{in}^{air} \in [0, 1]$, and of the middle case are shown on the left hand side in Fig. 6. The collocated results, namely the mean and the variance of the total vorticity are shown on the right hand side in the same figure.

The evolution of the PDF of total vorticity as a function of time is shown in Fig. 7.

The vorticity generation in a shock-bubble interaction can be divided into different stages with respect to time, and in the early times the primary vorticity deposition is the main mechanism in vorticity generation. The primary vorticity deposition is mainly based on baroclinic vorticity generation, which is due to the misalignment of the pressure gradient and the density gradient when the shock traverses the bubble [9]. As in our air-helium shock-bubble interaction, the baroclinic vorticity generation occurs from $t = 0 - 60\mu s$ as the shocks sweeps through the windward side of the bubble.

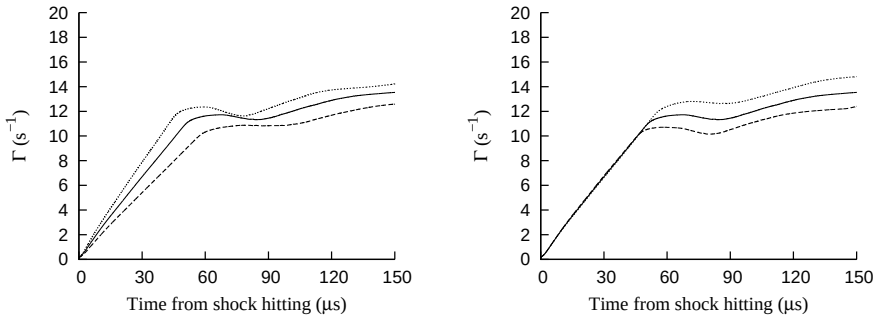

FIGURE 8. Total vorticity under other uncertainty parameters [1]. Left: individual cases under $f_{mass}^{air} \in [5.87\%, 48.38\%]$: dashed line – $f_{mass}^{air} = 48.38\%$, solid line – $f_{mass}^{air} = 28.45\%$, dotted line – $f_{mass}^{air} = 5.87\%$. Right: individual cases under $e \in [-0.5, +0.5]$: dashed line – $e = -0.5$, solid line – $e = 0$, dotted line – $e = +0.5$.

First, under the uncertainty parameter f_{in}^{air}, the statistic of the total vorticity is obtained and it can be seen that the variance of total vorticity increases from $t = 0 - 60\mu s$ and maintains approximately the same magnitude thereafter, as shown in Fig. 6. The corresponding PDF evolution of the total vorticity is shown in Fig. 7.

Second, when we compare the total vorticity under different uncertainty parameters, the initial condition of the bubble varies and thus the baroclinic vorticity generation also differs. For f_{mass}^{air}, as shown in Fig. 8, the different amounts of air in the bubble in the range of f_{mass}^{air} results in different density gradients, and the rates of baroclinic vorticity generation are therefore different. The increase of total vorticity also bottoms out at different time instants in the range of f_{mass}^{air}. For e, as shown in Fig. 8, the pressure gradient and the density gradient are the same in the range of e, but the misalignment of the gradient differs slightly due to the elliptical curvature. However, the difference in the misalignment of the gradients in the range considered does not have a significant effect on the rates of baroclinic vorticity generation. They are almost indistinguishable up to $t =\sim 50\mu s$. The main difference in the baroclinic vorticity generation is actually the streamwise extension of the bubble, where for an elliptical bubble with its major axis along the streamwise direction ($e = +0.5$), there is a longer length for baroclinic vorticity generation and thus a higher total vorticity. For f_{in}^{air}, as shown in Fig. 6, the rate of baroclinic vorticity generation is found to be higher for a higher gas inhomogeneity (along the spanwise direction), where the total amount of air in the bubble remains the same in the range f_{in}^{air}. Based on the extreme case under f_{in}^{air} where a maximum gas inhomogeneity is assumed, when we go further to study the cases in which the gradient of gas inhomogeneity changes to streamwise (+ve and -ve) direction, the rate of baroclinic vorticity generation exhibits a combined behavior as shown in Fig. 9.

5. Conclusions

We have extended our previous uncertainty quantification study on shock-bubble interactions to a new uncertainty parameter, namely the inhomogeneity of the contaminating gas in the bubble. The statistic of the interface evolution and total vorticity under this new uncertainty parameter is obtained and discussed. The vortex position of the rolled-up bubble is found to be the region of the maximum variance of density and the variance in the initial bubble is found to be transported and amplified as the interface evolves. The

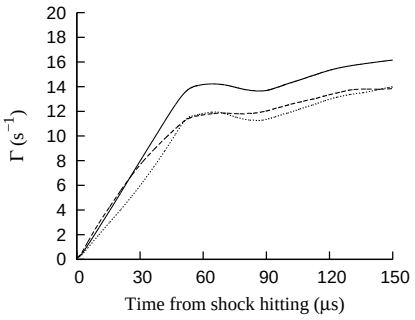

FIGURE 9. Total vorticity under different directions of the gas inhomogeneity gradient. Dashed line – gas inhomogeneity gradient pointing streamwise direction (+ve), solid line – gas inhomogeneity gradient pointing spanwise direction, dotted line – gas inhomogeneity gradient pointing streamwise direction (-ve).

results of the new uncertainty parameter are compared with those of other uncertainty parameters studied in our previous work, and the baroclinic vorticity generation under different initial bubble conditions is discussed. As compared with the analytical and numerical analysis of baroclinic vorticity production for a homogeneous circular bubble in shock-bubble interaction in reference literature, the baroclinic vorticity generation during the vorticity deposition phase is found to be largely dependent on the gas inhomogeneity inside the bubble and the windward length of the bubble when uncertainties of the initial bubble condition are present.

Acknowledgments

Financial support has been provided by the German Research Foundation (Deutsche Forschungsgemeinschaft – DFG) in the framework of the Sonderforschungsbereich Transregio 40 and the IGSSE (International Graduate School of Science and Engineering) at Technische Universität München.

References

[1] SO, K. K., CHANTRASMI, T., HU, X. Y., WITTEVEEN, J. A. S., STEMMER, C., IACCARINO, G. AND ADAMS, N. A. (2010) Uncertainty analysis for shock-bubble interaction. In: *Proc. CTR Summer Program 2010*, 15–26.

[2] SHANKAR, S. K., KAWAI, S. AND LELE, S. K. (2011). Two-dimensional viscous flow simulation of a shock accelerated heavy gas cylinder. *Phys. Fluids*, **23**(2).

[3] LAYES, G., JOURDAN, G. AND HOUAS, L. (2009). Experimental study on a plane shock wave accelerating a gas bubble. *Phys. Fluids*, **21**(7).

[4] HAAS, J. F. AND STURTEVANT, B. (1987). Interaction of weak shock waves with cylindrical and spherical gas inhomogeneities. *J. Fluid Mech.*, **181**, 47–76.

[5] SHANKAR, S. K., KAWAI, S. AND LELE, S. K. (2010). Numerical simulations of multicomponent shock accelerated flows and mixing using localized artificial diffusivity method. *AIAA 2010–352*.

[6] GREENOUGH, J. A., BECKNER, V., PEMBER, R. B., CRUTCHFIELD, W. Y., BELL, J. B. AND COLELLA, P. (2006). An adaptive multifluid interface-capturing method for compressible flow in complex geometries. *AIAA 95–1718*.

[7] TORO, E. (Ed.) (1997). *Riemann Solvers and Numerical Methods for Fluid Dynamics*. Springer.
[8] QUIRK, J. J. AND KARNI, S. (1996). On the dynamics of a shock-bubble interaction. *J. Fluid Mech.*, **318**, 129–163.
[9] SAMTANEY, R., RAY, J. AND ZABUSKY, N. J. (1998). Baroclinic circulation generation on shock accelerated slow/fast gas interfaces. *Phys. Fluids*, **10**(5).